FULL PAPER

Solar Absorber Gel

ADVANCED
ENERGY
MATERIALS

www.advenergymat.de

Solar Absorber Gel: Localized Macro-Nano Heat Channeling for Efficient Plasmonic Au Nanoflowers Photothermic Vaporization and Triboelectric Generation

*Minmin Gao, Connor Kangnuo Peh, Huy Thong Phan, Liangliang Zhu, and Ghim Wei Ho**

Plasmonic nanoparticles with outstanding photothermal conversion efficiency are promising for solar vaporization. However, the high cost and the required intense light excitation of noble metals, hinder their practical application. Herein, an inexpensive 3D plasmonic solar absorber gel that embraces all the desirable optical, thermal, and wetting properties for efficient solar vaporization is reported. The broadband absorption and strong near-field intertip enhancement of the sparsely dispersed gold nanoflowers contribute to efficient light-to-heat conversion, while the macro-nano thermal insulative silica gel retains and channels the plasmonic heat directly to the water pathways contained within the porous gel. The plasmonic-based solar absorber gel shows a vaporization efficiency of 85% under solar irradiation of 1 sun intensity (1 kW m^{-2}). Moreover, the porous gel framework exhibits high mechanical stability and antifouling properties, potentially useful for polluted/turbid water evaporation. Complementary water condensation-induced triboelectricity can be harvested alongside fresh water condensate, granting simultaneous fresh water production and electricity generation functionalities. The facile sol-gel synthesis at room temperature makes the solar absorber gel highly adaptable for practical large-scale photothermal applications.

1. Introduction

Solar energy is a promising renewable source for managing future energy demand. Efficient harvesting of solar energy and conversion to clean energy sources for human activities is essential for long-term sustainable development and environmental

Dr. M. Gao, Dr. C. K. Peh, Dr. L. Zhu, Prof. G. W. Ho
Department of Electrical and Computer Engineering
National University of Singapore
4 Engineering Drive 3, Singapore 117583, Singapore
E-mail: elehgw@nus.edu.sg
H. T. Phan, Prof. G. W. Ho
Engineering Science Programme
National University of Singapore
9 Engineering Drive 1, Singapore 117575, Singapore
Prof. G. W. Ho
Institute of Materials Research and Engineering
A*STAR (Agency for Science, Technology and Research)
2 Fusionopolis Way, Singapore 138634, Singapore

The ORCID identification number(s) for the author(s) of this article can be found under https://doi.org/10.1002/aenm.201800711.

protection. The solar industry covers an extensive range of applications, including photovoltaics, artificial photosynthesis, and solar thermal technology.[1] Among these applications, solar thermal energy, with the most efficient form of conversion, has been extensively used for solar hot water systems.[2] In recent years, utilizing solar energy to heat water for steam generation or water purification using nanostructured solar absorbers has drawn tremendous attention because of its potential to provide power and/or clean water.

Nanoplasmonic materials, with high optical absorption, exhibit localized heating typically in the immediate surrounding of tens of nanometers in water,[3] hence displays poor far-field heat translation/retention. A certain extent of heat insulation is imperative for effective plasmonic solar vaporization. The current interfacial vaporization design involves a floating solar absorber to absorb light irradiation, creating a hot concentrated region with an optional insulation layer introduced below the solar absorber layer to function as a thermal barrier.[4] Such an interfacial vaporization system confines the heat at the water–air interface which suppresses heat loss to the bulk water. However, the interception of the physical thermal barrier may compromise the effectiveness of capillary wicking of water of the solar absorber to hot spots for continuous steam generation.[5] Also, it is challenging to integrate all the desired optical, thermal, and wetting properties into a material system, thus multilayered structures with different functionalities are widely adopted.[4b,d,6] Often the incohesiveness and incompatibilities of the multilayered materials and interfaces are disregarded which may result in optical/heat losses, instability, and synthesis complexity trade-offs. Moreover, the current plasmonic interfacial vaporization design employs noble metal nanoparticles that typically absorb one or a few particular narrow wavelengths, which greatly limit the efficiency for solar thermal conversion. Although various approaches have been developed to enhance the light absorption of the plasmonic solar absorber, such as creating nanostructured arrays on optical substrates[7] and assembling compact nanostructures for light coupling,[8] these systems generally suffer from high cost due to the large

amount of noble metal used and the complicated fabrication process.

Therefore, in order to take practical advantage of the exceptional photothermal conversion efficiency of the plasmonic localized heating, it is essential to minimize the amount of noble metal usage, broaden the light absorption, and reduce heat loss to achieve high vaporization under 1 sun. Other than the common practice of introducing macroscopic heat isolation at the water–air interface, the heat insulation down to the nanoscopic water–solar absorber material interface primarily at the immediate surrounding of the solar absorber has been overlooked. Hence, the cooperative coupling of high optical absorption and effective macro-nano heat insulation of solar absorber material remains elusive.

In this work, we have demonstrated the first ever solar absorber gel comprising of sparsely dispersed AuFs at ppm concentration in a nanoporous silica matrix that shows efficient plasmonic solar vaporization. Contrary to the previous works on compact plasmonic metal solar absorber scheme, herein the intertips plasmon electric field coupling of an individual AuFs is capitalized to generate intense broadband heat coupled with nanoscopic heat insulation for sustaining elevated heat. This strategy has not been investigated before, which unprecedentedly reveals the superiority of the multiple tip AuFs and macro-nanoscale heat insulation for dilute plasmonic solar heating. Moreover, the all-embracing integral design of the inexpensive composite gel possesses key features for efficient solar vaporization which entails broadband absorption, macro-to-nanoscopic thermal insulation, and mesopores water capillary promotion and steam permeability. We achieve an evaporation efficiency of ≈85% under practical 1 sun irradiation. Notably, the 3D open network allows the passage of fluid while blocking off certain dissolved and particulate matters. This attribute offers the possibilities of passive filtering and antifouling capabilities especially useful when performing solar water vaporization using turbid water source. Subsequently, we demonstrated the first ever integral prototype design for parallel production of fresh water and triboelectricity through water evaporation distillation process. This synergistic capability of distillate production and energy generation addresses clean water-energy solutions.

2. Results and Discussion

A schematic drawing of the designed solar absorber gel for solar vaporization is shown in **Figure 1**. The floating gel consists of AuFs as the solar thermal collector tailored for efficient light harvesting. The AuFs demonstrate broadband absorption of almost the whole visible to near-infrared (NIR) region, while silica gel is transparent in this region so as to not interfere the light absorption of the AuFs. Moreover, AuFs with numerous tips enhance the electromagnetic field without the need to aggregate particles.[9] This enhancement within each individual AuFs not only translates to enhanced plasmonic localized heat generation, but also significantly lowers the utilization of precious noble metal. Furthermore, the open mesoporous structure of the solar absorber gel with controllable pore sizes provides the capillary water transport channels and steam pathways (Figure 1B), while filtering off the natural particulates, such as dust, sand, bacteria in fresh water (Figure 1A). In addition, the 3D silica gel with low thermal conductivity provides macroscopic insulation that prevents the heat loss to bulk water (Figure 1A) and at the same time, the nanosized silica particles enwrap the well-dispersed AuFs for nanoscopic heat confinement for efficient solar vaporization (Figure 1B).

The solar absorber gel was synthesized by incorporating plasmonic AuFs (Figure S1A,B, Supporting Information) into silica hydrogel using a one-step base catalyzed coprecursor sol-gel chemistry at room temperature. The schematic diagram of the synthetic process is shown in **Figure 2**A (see Materials Synthesis, Supporting Information) The AuF solution was functionalized with polyvinylpyrrolidone (PVP) to prevent agglomeration and to act as the bridging molecule for incorporating metallic nanomaterials into silica gel network while retaining the gel structure.[10] By adopting the coprecursor system, the nonhydrolyzable methyl groups ($RSi–CH_3$) of methyltrimethoxysilane (MTMS) are attached to the silica cluster formed by tetraethyl orthosilicate (TEOS) monomers after sufficient hydrolysis, the whole gelation process takes less than 10 min. The interaction between the two precursors of the silica gel was studied using Fourier transform infrared (FTIR), where the presence of organic $RSi–CH_3$ group confirms the formation of TEOS-MTMS hybrid silica gel (see Note S1, Figure S2,
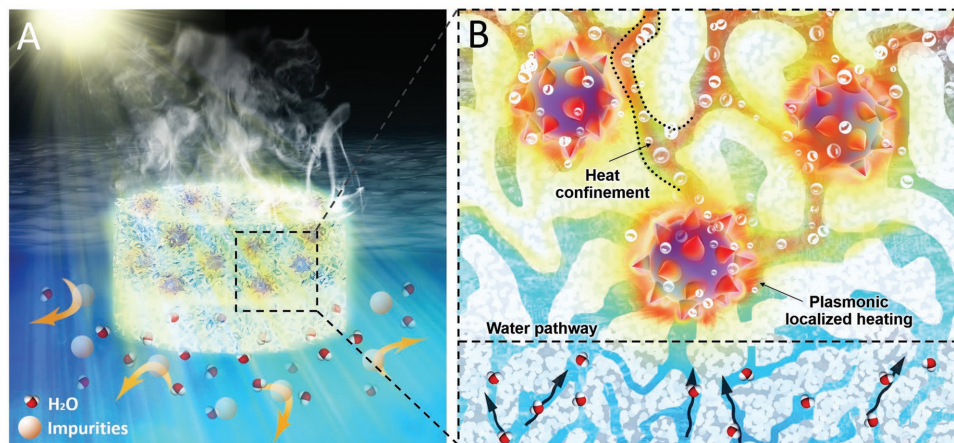

Figure 1. Schematic drawing of the designed solar absorber gel for solar vaporization. A) Macroscopic view. B) Nanoscopic view.
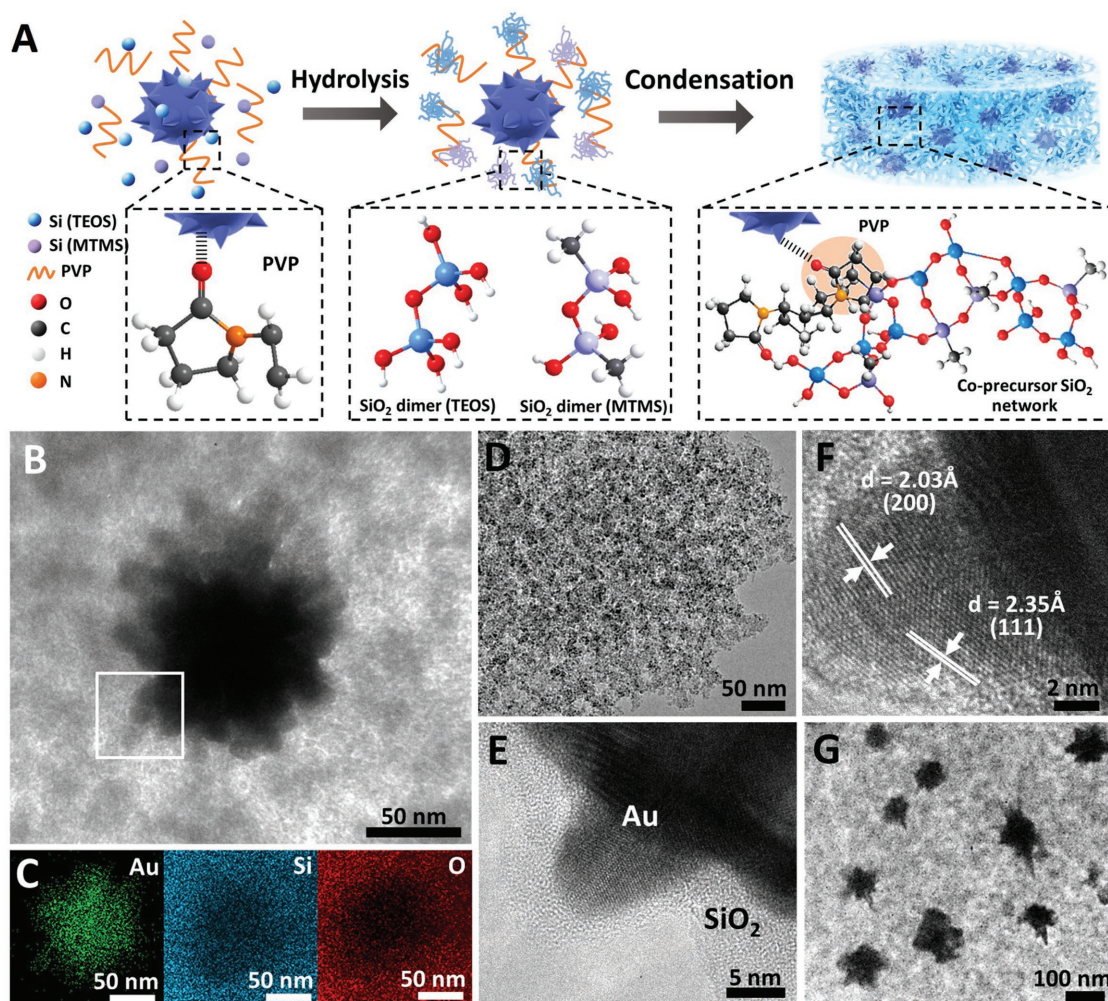
Figure 2. A) Schematic diagram of the synthetic process of the solar absorber gel. B) TEM image and C) EDX mapping of AuF silica gel. D–F) High-resolution TEM images of crystalline AuF within the amorphous porous SiO₂ matrix. G) TEM image of sparsely dispersed AuFs in silica gel.

Supporting Information). The inorganic–organic hybrid silica gel possesses larger surface area (809 m² g⁻¹) with uniform pore size of ≈3.5–4 nm, as compared to the single precursor (TEOS) system (521 m² g⁻¹) with a broad pore size distribution from 3 to 15 nm (see Note S2, Figures S3 and S4, Supporting Information) This mesoscopic open gel network is favorable for capillary flow. Moreover, its highly organized uniform porosity is beneficial for filtering purpose and resisting the lateral compressive stresses.[10,11] With the presence of PVP in the composite gel, hydrogen bonds are formed between hydroxyl groups of sol-gel oxides and carbonyl groups in the polymer chain which further improve its mechanical properties and flexibility.[12] The structure of the composite gel was examined using transmission electron microscopy (TEM), and a good interface and continuity between the well-preserved AuF structure and the mesoporous silica gel can be observed (Figure 2B). The energy-dispersive X-ray (EDX) elemental mappings (Figure 2C) correspond to Au M-edge, Si K-edge, and O K-edge element, respectively, with strong Au signal located at the center and the Si and O signals throughout the scanning area. The high-resolution TEM images further reveal the confinement of crystalline AuF within

the amorphous porous SiO₂ matrix (Figure 2D, and Figure S5, Supporting Information) even at the ≈10 nm nanometer flower tip (Figure 2E). The lattice fringes of 2.03 and 2.35 Å correspond to the (200) and (111) planes of metallic Au, respectively (Figure 2F). The successful incorporation of well-retained, sparsely dispersed AuFs nanostructures into the transparent silica matrix (Figure 2G) not only allow efficient water transport and steam flow, but also enable pronounced plasmonic light harvesting and nanoscale insulation at the heat generation vicinity.

The light absorption capability of the AuFs solution is compared with the commonly adopted Au nanoparticles (AuPs) solar absorber material (**Figure 3**A). The AuFs with multiple tips display broadband absorption with distinctive plasmonic resonance peaks in both visible (at ≈680 nm) and NIR (at ≈998 nm) region. Compared with AuPs solution which only exhibits a rather narrow absorption at ≈520 nm, the AuFs possess extraordinary high absorbance across a wider range. Previous works have already proven both experimentally and theoretically that nonspherical metal nanostructures facilitate a stronger localization of electromagnetic energy due to the anisotropic distribution
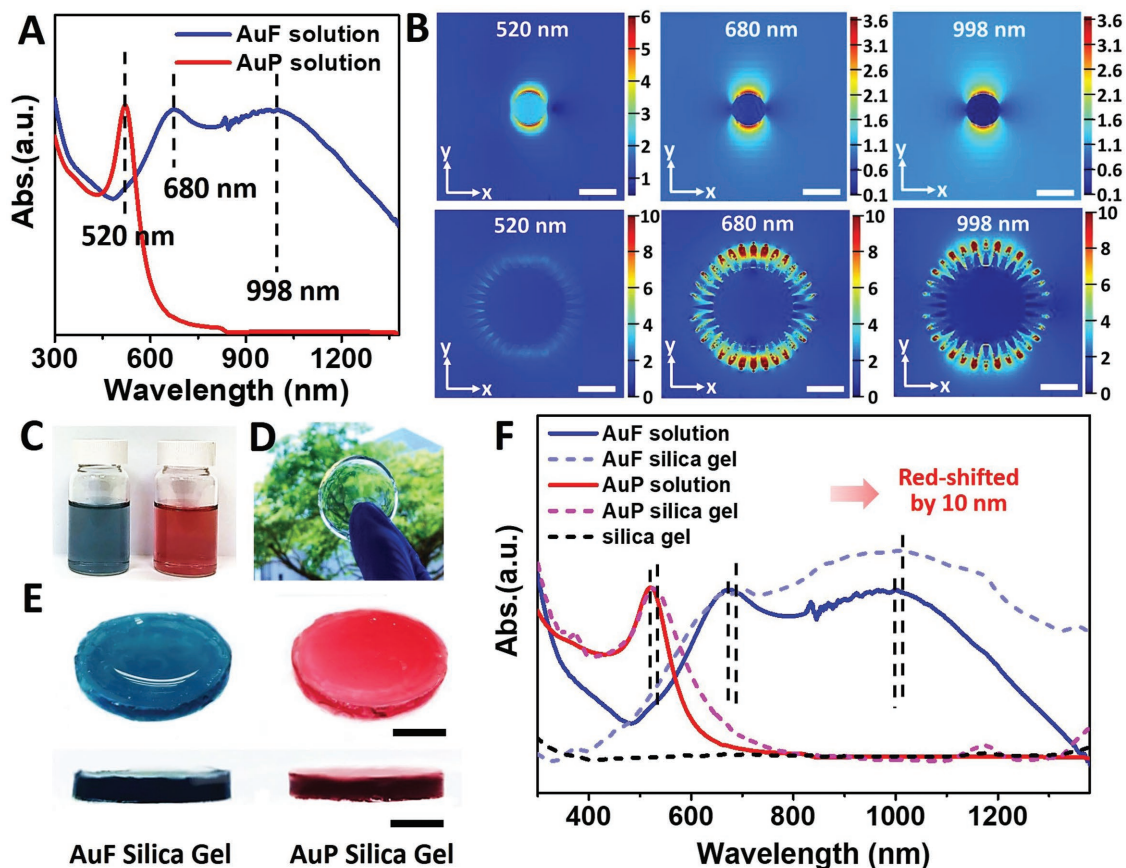
Figure 3. A) UV–vis spectra of AuP and AuF solutions. B) Near-field enhancement maps of AuP (scale bar: 60 nm) and AuF (scale bar: 30 nm) at wavelength of 520, 680, and 998 nm. C–E) Digital photo of AuP and AuF solutions, transparent silica gel, and AuP and AuF silica gel (scale bar: 1 cm). F) UV–vis spectra of AuP and AuF silica gels compared with AuP and AuF solutions.

of the electromagnetic field at the tips.[9a,13] In this work, electromagnetic simulations were also performed (see Note S3, Figure S6, Supporting Information). It is well established that the intrinsic properties of multiple tip Au nanoparticles exhibit both longitudinal and transverse plasmon resonance correspond to the tips (at 998 nm) and the center core (at 680 nm), respectively.[14] Additionally, the plasmon resonance confined within the tips dominate the overall optical response as shown in the near-field enhancement maps (Figure 3B). Three different wavelengths were selected based on the resonance bands of AuPs (520 nm) and AuFs (680 and 998 nm). The near-field enhancement maps reveal the dipolar oscillation confined within the core of AuPs at the resonance peak of 520 nm (Figure 3B top), and the intertip interaction of AuPs at both 680 and 998 nm (Figure 3B bottom). This tip enhancement allows strong light coupling among the tips without enforcing close-packing/assembling of nanoparticles.[9,15] The pronounced light absorption of the AuFs with broadband absorption and yet well-defined plasmonic resonance band in both visible and NIR region make it a promising plasmonic solar absorber.

The AuPs and AuFs solution (Figure 3C, AuFs: blue solution, AuPs: red solution) was used for composite gel formation. The concentration was normalized based on the absorption peaks (Figure 3A). The pure silica gel is transparent (Figure 3D), while the composite gels with the incorporated AuFs and AuPs

(ppm level) display blue and red colored gels, respectively (Figure 3E). AuP silica gel was used as a reference sample for solar vaporization performance comparison, as most of the published works adopted AuPs as a plasmonic solar absorber.[6a,c,16] The average size of the AuPs used for composite gel is ≈30 nm (Figure S7, Supporting Information) and TEM reveals the successful inclusion of AuPs into the silica matrix with a similar dispersion as the AuFs silica gel (Figure S8, Supporting Information). X-ray diffraction (XRD) confirms the hybrid composition with a broad peak at 23° that corresponds to the amorphous silica, while diffraction peaks at 38.1°, 44.3°, and 64.5° are assigned to Au (111), (200), and (220) (Figure S9, Supporting Information). The optical properties of the composite gels were examined using UV–vis spectroscopy to investigate the effect of silica on overall light-harvesting capability. The absorption spectrum of the composite gel is observed to redshift (Figure 3F). This is due to an increase in the refractive index near the surface of the Au nanostructure from water to silica.[17] The mesoporous silica matrix is chosen not only because of its structural advantages for capillary flow as discussed earlier, but also in view of its desirable optical properties. It is highly transparent in both visible and NIR region (400–1200 nm) (Figure 3F), which allows the uninterrupted solar transmission and absorbance by the plasmonic solar absorber. Additionally, there are some absorption peaks associated with the silica in
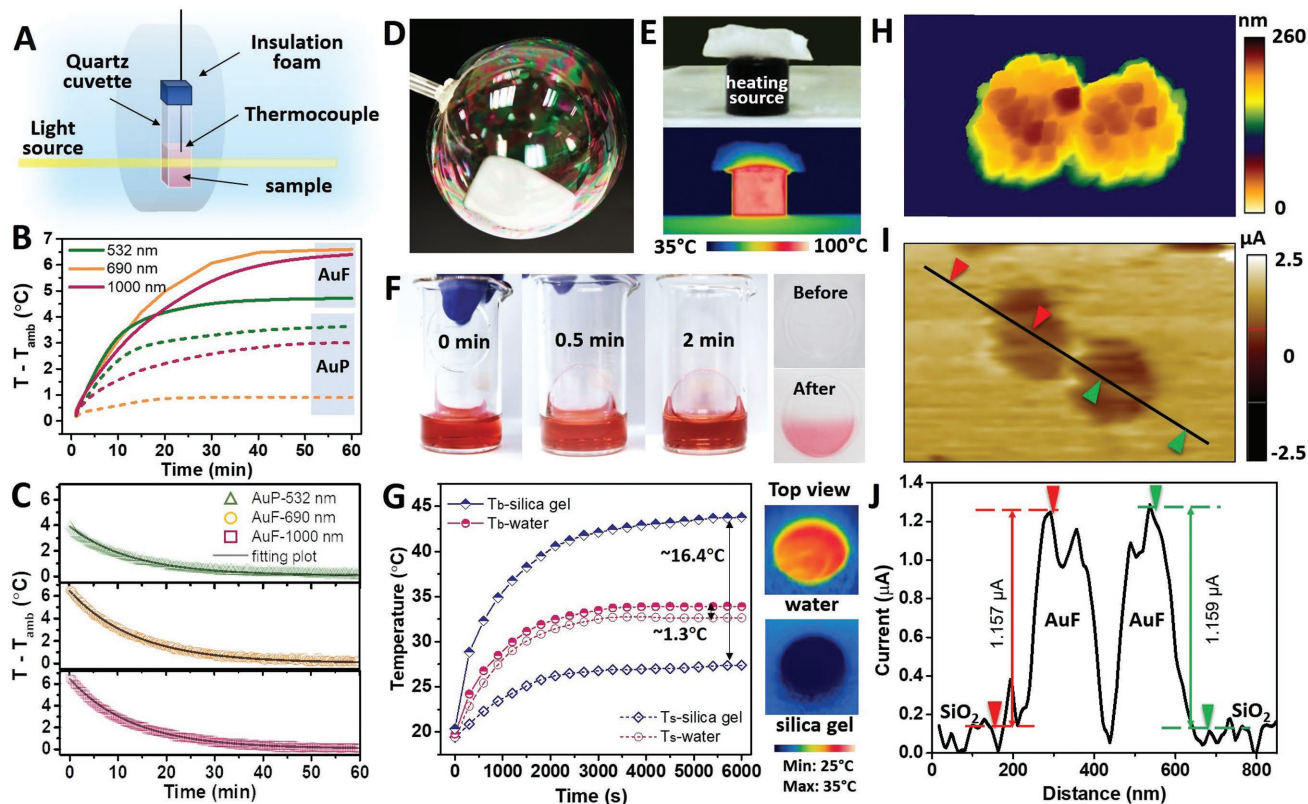
Figure 4. A) Schematic drawing of the setup for photothermal conversion efficiency measurement. B,C) Temperature rising profiles with time of AuP and AuF solutions under laser irradiation (100 mW) at different wavelengths of 532, 690, and 1000 nm and the temperature cooling profiles. D) Digital photo of silica aerogel in elastic plastic bubble. E) Digital photo of thermal insulation test with the silica aerogel on a heating source (top) and the respective thermographic image (bottom). F) Digital photos of solvent exchange experiment with pure silica gel. G) Temperature profiles of the thermal insulation test with silica gel and water at the top surface (T_s) and the bottom of the material in contact with the heater (T_b). H) AFM topography image of AuF on silica gel using QI mode. I,J) SThM image using conductivity contrast microscopy and the probe current signal profile along the black line of the two AuFs on silica gel.

the infrared region between 1300 and 2500 nm which further broaden the overall solar absorbance (Figure S10, Supporting Information).

In order to design efficient plasmonic absorber for photothermal applications, the key factors lie in both broadband solar absorption and efficient conversion of solar-to-thermal energy. Plasmonic nanoparticles with much larger light absorption cross section than the physical size under resonance excitation possess extraordinary photothermal conversion efficiency owing to its localized plasmon resonance that confines light at nanoscale.[6a,18] To examine the photothermal conversion efficiency, a setup (**Figure** 4A, Note S4, Supporting Information) was used to measure the heating and cooling temperatures of the AuPs and AuFs solution as a function of time at various wavelengths corresponding to their resonance bands (Figure 4B). The calculated values for heat loss fit well with the experimental data as shown in Figure 4C and Figure S11 (Supporting Information). These values were used together with the maximum temperature achieved above ambient temperature for the photothermal conversion efficiency calculations (see Note S5, Supporting Information).[19] The calculated effective photothermal conversion efficiencies of AuFs (47.3% at 532 nm, 78.5% at 690 nm, 76.6% at 1000 nm) are higher than AuPs (37.2% at 532 nm, 7.7% at 690 nm, Nil at 1000 nm

due to its negligible light absorption) at all chosen wavelengths (see Note S6, Figure S12, Supporting Information) Based on both the optical and the photothermal characterizations, the AuFs not only exhibit broadband absorption, but also surpass AuPs in terms of photothermal conversion efficiency. These are the basis of using AuFs over AuPs as solar absorber materials which will translate into higher solar vaporization.

Besides broadband absorption and high photothermal conversion efficiency, another factor that also plays an essential role in solar vaporization is the thermal properties of the system to minimize heat loss at both macro and nanoscale level. In our design, silica gel with low thermal conductivity is judiciously used as both the floating platform for air–water interfacial solar heating and the insulation layer to minimize heat loss. It is well known that silica aerogel is extremely lightweight (Figure 4D) due to its highly porous structure with air trapped in cavities. Aside from the porous structure, the intrinsic property of low thermal conductivity contributes to the excellent thermal insulation as demonstrated by placing the silica aerogel on a heating source (Figure 4E, top). The thermographic image reveals the thermal insulation of the silica gel in the radial direction (Figure 4E, bottom),[20] with the temperature difference between the bottom and the top of the silica gel to be ≈50 °C (Figure S13, Supporting Information). In this work, the mesoporous solar

**ADVANCED
SCIENCE NEWS**

www.advancedsciencenews.com

**ADVANCED
ENERGY
MATERIALS**

www.advenergymat.de

absorber gel that provides the pathways for both water and steam flow can be directly used for solar vaporization without undergoing any drying process. The solvent exchange experiment (Figure 4F) demonstrates that the gel (colored with dyes for visualization) can easily wick the water within seconds, while the reverse process of colored water desorption and replacement with pure water is shown in Figure S14 (Supporting Information). This silica gel also possesses good insulation properties, even though it may not be as superior as silica aerogel due to the presence of water. A similar experiment (see Note S7, Figure S15, Supporting Information) has been carried out where the temperature difference between the top and the bottom of silica gel (16.4 °C) is much higher than water (1.3 °C) as shown in Figure 4G. This suggests that silica gel filled with water still warrants superior thermal insulation compared to water. The silica gel effectively insulates the heat transfer from the heating source to the top of the sample while sustaining high temperature in the vicinity of the heating source. This property suggests that the silica gel not only minimizes the heat loss to the bulk water and the surrounding at the macroscopic level, but also confines the heat generated by the AuFs at the solar absorber material–water interface as the AuFs solar thermal collector is capsulated inside the silica gel. This localized heat confinement effect at the nanoscale level is then examined using scanning thermal microscopy (SThM) based on contact mode of atomic force microscopy (AFM) technique.[21] The AuFs with silica gel at the bottom was probed by AFM quantitative imaging (QI) mode (Figure 4H). Similar area as presented in QI mode was chosen for conductivity contrast microscopy (CCM) imaging using the nanothermal probe (Figure S16, Supporting Information, and Figure 4I). The apparent probe current signal (ΔI) of the two individual AuFs and the silica gel layer underneath can be detected with a set probe voltage of 250 mV heating the probe tip (Figure 4J). It can be seen that the differences between the AuFs and the silica are consistent for the chosen particles which reveal the distinctive thermal conductivities between the metallic Au and insulative silica gel. Therefore, the solar absorber gel possesses excellent insulation properties to the macroscopic and nanoscopic extent for efficient heat transfer to the desired water/vapor pathways.

Notably, the solar absorber gel combines all desirable optical, thermal, and wetting properties in an integral design for solar-driven vaporization. Collectively, (i) AuFs function as the efficient solar absorber material with broadband absorption and high photothermal conversion efficiency, (ii) transparent silica gel supporting structure contributes to the extended light absorption, and (iii) porous silica gel serves as water/steam transport channels while providing crucial thermal insulation at both macro and nanoscale level. To explore the influence of both AuFs solar absorber and the silica gel matrix on solar vaporization, different systems (**Figure 5**A and Figure S17, Supporting Information) are studied and compared with pure water evaporation. First, three different systems were chosen, namely, pure silica gel (Figure S17A, Supporting Information), AuP silica gel (Figure S17B, Supporting Information), and AuF silica gel
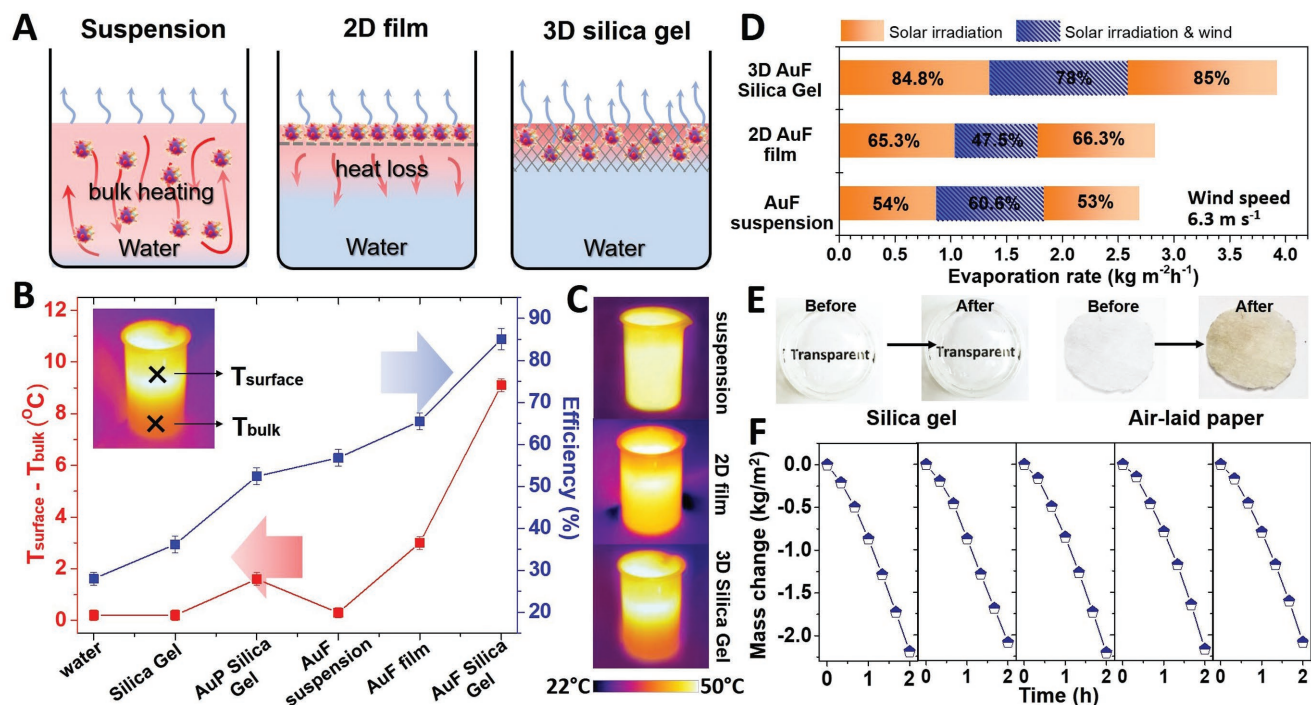

Figure 5. A) Schematic diagram of AuF suspension, 2D film, and 3D silica gel systems. B) The evaporation efficiencies and the temperature differences between the surface ($T_{surface}$) and the bulk water (T_{bulk}) for various systems under 1 sun (1 kW m^{-2}). C) The thermographic images of the three systems in (A) under solar irradiation. D) The evaporation rates and efficiencies of the three systems in (A) under 1 sun with and without the wind. E) Digital photos of the antifouling test of silica gel and air-laid paper before and after soaking in rainwater collected from the ground. F) Stability and reusability of AuF silica gel for solar vaporization.

**ADVANCED
SCIENCE NEWS**
www.advancedsciencenews.com

**ADVANCED
ENERGY
MATERIALS**
www.advenergymat.de

(Figure S17D, Supporting Information) to study the optical properties of the composite gel. The water evaporation rates of the three systems under solar irradiation (1 kW m^{-2}) were determined to be 0.576, 0.834, and 1.356 kg m^{-2} h^{-1}, respectively which correspond to the conversion efficiencies of ≈36, 52, and 85% (see Notes S8 and S9, Figures S18 and S19A, Supporting Information, and Figure 5B). The temperature differences between the surface of the sample ($T_{surface}$) and the bulk water (T_{bulk}) were calculated based on the measurements shown in Figure S19 (Supporting Information). This temperature difference is an indicator for interfacial heating effect at the air–water interface. Both AuF and AuP silica gel perform better than pure transparent silica gel due to the presence of solar absorber materials. Notably, the AuF silica gel outperforms the AuP silica gel by ≈63%. The enhancement is clearly attributed to the broadband absorption and higher photothermal conversion efficiency of AuF since both systems have the same insulation and capillarity properties.

Next, the thermal insulation properties of the composite gel for solar evaporation were examined. Currently, the most efficient approach to minimize heat loss on the macroscopic level is based on solar heating at the air–water interface, and the commonly adopted system of loading the plasmonic solar absorber material on 2D paper-like floating structures.[6a–c,16a,b,22] Although this system reduces heat loss as opposed to a volumetric heating system where the nanoparticles are dispersed in bulk solution, thermal diffusion through both conduction and convection to the nonevaporative portion under the floating structure is inevitable. The effectiveness of this "air–water interface" heating with thermal insulation properties was verified by comparing the 2D AuF film and the 3D AuF silica gel with traditional AuF suspension system (schematic drawings in Figure 5A). The 2D AuF film is prepared by casting the same amount of AuFs used in the silica gel onto a polytetrafluoroethylene (PTFE) filter paper forming a uniform 2D AuF film (Figure S20, Supporting Information). The solar evaporation efficiencies of various samples prepared for all the three different systems are tested and the results (Figure S21, Supporting Information) show that the solar evaporation efficiency is highly reproducible across different samples for each system with standard deviation of ≈2%. The solar evaporation efficiencies of both the 2D AuF film and the 3D AuF silica gel systems are higher than the suspension system with ≈15 and ≈49% enhancement, respectively (see Note S10, Supporting Information). Although the 2D film system does prevent heat loss to the bulk water based on "air–water interface" heating, the insulation is not as good as the silica gel. This can be seen from the temperature profile of the bulk water heating as shown in Figure 5C and Figure S19B (Supporting Information). The temperature difference of the 2D AuF film between the surface and the bulk is only 3.0 °C which is significantly lower than that of the 3D AuF silica gel of 9.1 °C (Figure 5B). It is also observed that the surface temperature of 3D AuF silica gel is almost ≈5 °C higher than the 2D AuF film. This is contributed by the heat confinement effect of the silica gel at both macroscopic and nanoscopic level, thus leading to a higher evaporation efficiency of 85.1% compared with 2D AuF film system (65.5%). In addition, this 3D porous silica gel matrix also provides more accessible area for steam formation relative

to the widely adopted 2D substrate/film system which is limited in the surface area.[6d,22,23]

To further attest the insulation properties of the 3D AuF silica gel, wind with a flow rate of 6.3 m s^{-1} was introduced to the system to simulate a real environment for practical solar vaporization applications. There is an obvious drop of 28.3% in the water evaporation efficiency of 2D AuF film in the presence of wind. In contrast, the evaporation efficiency of 3D AuF silica gel was reduced by only 8.0% in spite of a higher surface temperature, making it more susceptible to heat loss with wind exposure (Figure 5D). These results validate the excellent thermal insulation properties of the 3D composite gel compared with 2D AuF film system. There are two effects of wind when introduced to the solar vaporization, that is, the reduction of surface and the environment temperature (Figure S22, Supporting Information), at the same time, an increase in air flow rate that results in faster evaporation rate due to efficient removal of generated water vapor, thus reduced the partial pressure of water in air close to the evaporation system. The latter effect is observed to dominate in the case of AuF suspension system. The temperature of the suspension system was less affected by the wind due to the larger thermal mass of the bulk heating system. Thus, the evaporation efficiency became even higher (≈60.6%) when the wind was introduced due to the reduced partial pressure of water in the air, compared with the same system subjected only to the solar irradiation (≈54%) (Figure S23, Supporting Information). However, the increased evaporation rate still falls behind the 3D AuF silica gel (≈84.8%). The overall average evaporation rate of AuF silica gel is 42% higher than AuF suspension system for both with and without wind conditions.

Finally, another factor that needs to be considered for practical application is its reusability and stability. The 3D porous silica gel with tailored uniform pore sizes of 3.5–4.0 nm is not only favorable for water and steam flow, but also rejects particulate, dirt, and naturally occurring organic matter in water. The antifouling effect has been tested by soaking different supporting materials overnight in the rainwater collected from the ground (Figures S24–S26, Supporting Information). The transparent 3D silica gel is used for better visualization without the color interference from the AuFs, and compared with the commonly adopted 2D paper systems, including low lint wipe, airlaid paper, and filter paper. The silica gel remains clear and transparent, while the other supporting materials show various degrees of fouling (Figure 5E and Figures S24–S26, Supporting Information). The AuF silica gel is also shown to be mechanically stable for reusability and recycling without obvious deterioration of water evaporation ability (Figure 5F). Furthermore, the AuFs encapsulated within the silica gel prevent dissolution and displacement from the supporting material.

A proof-of-concept prototype was built to collect the condensate from the solar evaporation of the water, as well as to harness triboelectric energy generated from the flow of condensate on a PTFE surface. The prototype consists of inclined walls and a round bottom vessel lined with PTFE energy harnessing triboelectric nanogenerator (TENG) devices (**Figure 6**A, and Figure S27, Supporting Information). The hydrogel is enclosed within the prototype, and light is directed through a window above the hydrogel. The water vapor condenses on the wall to form tiny
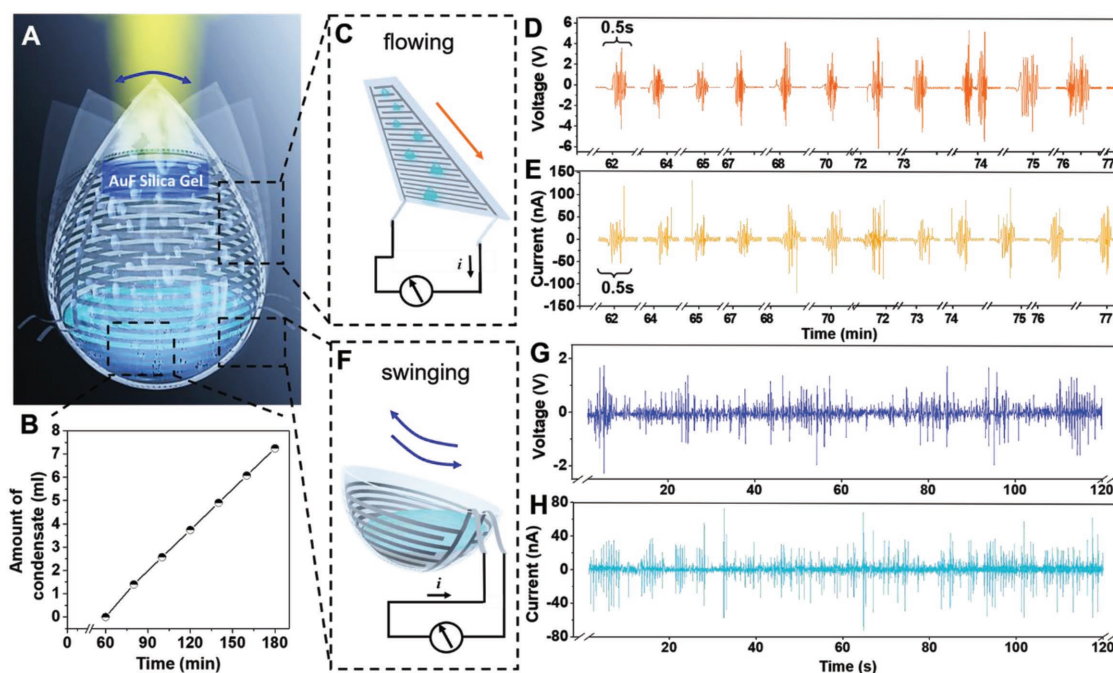
ADVANCED
SCIENCE NEWS
www.advancedsciencenews.com

ADVANCED
ENERGY
MATERIALS
www.advenergymat.de

Figure 6. A) Schematic diagram of the integral prototype for condensate collection and triboelectric energy generation. B) The condensate collected under focused sunlight after the first 60 min. C) Schematic diagram of triboelectric nanogenerator (TENG) for water flowing down the wall. D) Open-circuit voltage and E) closed-circuit current measurements of the TENG device shown in (C) with a sampling time of 15 min. F) Schematic diagram of triboelectric nanogenerator (TENG) for water swinging in the round bottom vessel. G) Open-circuit voltage and H) closed-circuit current measurements of the TENG device are shown in (F) with a sampling time of 2 min.

water droplets which then accumulate to become bigger water droplets that will overcome the friction of the wall surface and flow down due to gravity. The condensate is then collected at the bottom of the vessel (Figure 6B). The flow of the condensate generates electric signals (Figure 6C) due to the electrification of the water and the PTFE. The contact between water and PTFE causes the surface of the PTFE to be negatively charged, and the water droplet to be positively charged.[24] As the water droplet flows across the different individual electrodes, it induces the electrode to be more negatively charged, and the electrical potential between different electrodes causes a flow of electrons. The triboelectric signals due to the gravitational flow of condensate droplets off the walls are shown in Figure 6D,E. The corresponding power outputs with various external load resistances have been calculated (Figure S28, Supporting Information) and the maximum peak power obtained is 0.63 µW. Notably, the round-bottom prototype structure is purposefully designed to harness omnidirectional mechanical energy, for example, wind energy, to set it to swing in random directions. This in turn triggers the movement of the collected condensate inside the round bottom (Figure 6F) to generate triboelectric signals as well (Figure 6G,H). This integral device provides an innovative approach for parallel collection of water condensate and triboelectric energy during the solar evaporation process.

3. Conclusion

An inexpensive and scalable room-temperature synthesis of solar absorber gel with sparsely dispersed AuF (≈27.2 ppm) is

demonstrated. The 3D composite gel possesses all desirable properties for solar-driven vaporization in an integral scheme, including broadband absorption, high photothermal conversion, efficient fluid capillarity, and effective macro-nano heat insulation. With this design, the evaporation efficiency achieved under 1 sun is ≈85% and is three times higher than pure water evaporation under the same condition. Moreover, the precursor porous silica framework exhibits high mechanical stability and antifouling properties, endowing it with advantageous properties for practical steam generation using polluted/turbid water resources. The integral prototype design enables concurrent fresh water production and triboelectric energy generation through the solar evaporation distillation process. The solar absorber gel is not only promising for solar-driven evaporation, but also in other potential photothermal catalysis and desalination applications.

4. Experimental Section

Experimental details and specific characterization methods are described in the Supporting Information.

Supporting Information

Supporting Information is available from the Wiley Online Library or from the author.

Conflict of Interest

The authors declare no conflict of interest.

Keywords

[1] N. Kannan, D. Vakeesan, *Renewable Sustainable Energy Rev.* **2016**, *62*, 1092.

[2] P. V. Kamat, *J. Phys. Chem. C* **2007**, *111*, 2834.

[3] a) D. Boyer, P. Tamarat, A. Maali, B. Lounis, M. Orrit, *Science* **2002**, *297*, 1160; b) A. O. Govorov, H. H. Richardson, *Nano Today* **2007**, *2*, 30.

[4] a) H. Ghasemi, G. Ni, A. M. Marconnet, J. Loomis, S. Yerci, N. Miljkovic, G. Chen, *Nat. Commun.* **2014**, *5*, 4449; b) G. Ni, G. Li, S. V. Boriskina, H. Li, W. Yang, T. Zhang, G. Chen, *Nat. Energy* **2016**, *1*, 16126; c) X. Li, W. Xu, M. Tang, L. Zhou, B. Zhu, S. Zhu, J. Zhu, *Proc. Natl. Acad. Sci. USA* **2016**, *113*, 13953; d) Z. Liu, H. Song, D. Ji, C. Li, A. Cheney, Y. Liu, N. Zhang, X. Zeng, B. Chen, J. Gao, Y. Li, X. Liu, D. Aga, S. Jiang, Z. Yu, Q. Gan, *Global Challenges* **2017**, *1*, 1600003; e) L. Shi, Y. Wang, L. Zhang, P. Wang, *J. Mater. Chem. A* **2017**, *5*, 16212.

[5] Z. Deng, J. Zhou, L. Miao, C. Liu, Y. Peng, L. Sun, S. Tanemura, *J. Mater. Chem. A* **2017**, *5*, 7691.

[6] a) S. Yu, Y. Zhang, H. Duan, Y. Liu, X. Quan, P. Tao, W. Shang, J. Wu, C. Song, T. Deng, *Sci. Rep.* **2015**, *5*, 13600; b) C. Liu, J. Huang, C.-E. Hsiung, Y. Tian, J. Wang, Y. Han, A. Fratalocchi, *Adv. Sustainable Syst.* **2017**, *1*, 1600013; c) X. Wang, Y. He, X. Liu, G. Cheng, J. Zhu, *Appl. Energy* **2017**, *195*, 414; d) Y. Liu, S. Yu, R. Feng, A. Bernard, Y. Liu, Y. Zhang, H. Duan, W. Shang, P. Tao, C. Song, T. Deng, *Adv. Mater.* **2015**, *27*, 2768.

[7] a) X. Xiong, S.-C. Jiang, Y.-H. Hu, R.-W. Peng, M. Wang, *Adv. Mater.* **2013**, *25*, 3994; b) T. Søndergaard, S. M. Novikov, T. Holmgaard, R. L. Eriksen, J. Beermann, Z. Han, K. Pedersen, S. I. Bozhevolnyi, *Nat. Commun.* **2012**, *3*, 969.

[8] R. W. Taylor, R. Esteban, S. Mahajan, R. Coulston, O. A. Scherman, J. Aizpurua, J. J. Baumberg, *J. Phys. Chem. C* **2012**, *116*, 25044.

[9] a) L.-C. Cheng, J.-H. Huang, H. M. Chen, T.-C. Lai, K.-Y. Yang, R.-S. Liu, M. Hsiao, C.-H. Chen, L.-J. Her, D. P. Tsai, *J. Mater. Chem.* **2012**, *22*, 2244; b) A. S. D. S. Indrasekara, R. Thomas, L. Fabris, *Phys. Chem. Chem. Phys.* **2015**, *17*, 21133.

[10] J. P. Randall, M. A. B. Meador, S. C. Jana, *ACS Appl. Mater. Interfaces* **2011**, *3*, 613.

[11] a) Z. Li, X. Cheng, S. He, D. Huang, H. Bi, H. Yang, *Mater. Lett.* **2014**, *129*, 12; b) S. C. Warren, M. R. Perkins, A. M. Adams, M. Kamperman, A. A. Burns, H. Arora, E. Herz, T. Suteewong, H. Sai, Z. Li, J. Werner, J. Song, U. Werner-Zwanziger, J. W. Zwanziger, M. Grätzel, F. J. DiSalvo, U. Wiesner, *Nat. Mater.* **2012**, *11*, 460.

[12] a) G. J. Owens, R. K. Singh, F. Foroutan, M. Alqaysi, C.-M. Han, C. Mahapatra, H.-W. Kim, J. C. Knowles, *Prog. Mater. Sci.* **2016**, *77*, 1; b) H. Okumura, Y. Okamoto, *J. Phys. Chem. B* **2008**, *112*, 12038.

[13] a) L. Rodríguez-Lorenzo, R. de la Rica, R. A. Álvarez-Puebla, L. M. Liz-Marzán, M. M. Stevens, *Nat. Mater.* **2012**, *11*, 604; b) W. Kim, N. Kim, J. W. Park, Z. H. Kim, *Nanoscale* **2016**, *8*, 987.

[14] a) K. P. Senthil, P.-S. Isabel, R.-G. Benito, F. J. G. d. Abajo, M. L.-M. Luis, *Nanotechnology* **2008**, *19*, 015606; b) A. Kedia, P. S. Kumar, *RSC Adv.* **2014**, *4*, 4782.

[15] A. Maity, A. Maiti, P. Das, D. Senapati, T. K. Chini, *ACS Photonics* **2014**, *1*, 1290.

[16] a) K. Bae, G. Kang, S. K. Cho, W. Park, K. Kim, W. J. Padilla, *Nat. Commun.* **2015**, *6*, 10103; b) C. Chang, C. Yang, Y. Liu, P. Tao, C. Song, W. Shang, J. Wu, T. Deng, *ACS Appl. Mater. Interfaces* **2016**, *8*, 23412; c) L. Zhou, Y. Tan, D. Ji, B. Zhu, P. Zhang, J. Xu, Q. Gan, Z. Yu, J. Zhu, *Sci. Adv.* **2016**, *2*, e1501227.

[17] M. Gao, L. Zhu, W. L. Ong, J. Wang, G. W. Ho, *Catal. Sci. Technol.* **2015**, *5*, 4703.

[18] M. Gao, P. K. N. Connor, G. W. Ho, *Energy Environ. Sci.* **2016**, *9*, 3151.

[19] H. Chen, L. Shao, T. Ming, Z. Sun, C. Zhao, B. Yang, J. Wang, *Small* **2010**, *6*, 2272.

[20] B. Wicklein, A. Kocjan, G. Salazar-Alvarez, F. Carosio, G. Camino, M. Antonietti, L. Bergström, *Nat. Nanotechnol.* **2015**, *10*, 277.

[21] a) A. Soudi, R. D. Dawson, Y. Gu, *ACS Nano* **2011**, *5*, 255; b) S. Huxtable, D. G. Cahill, V. Fauconnier, J. O. White, J.-C. Zhao, *Nat. Mater.* **2004**, *3*, 298.

[22] L. Zhou, Y. Tan, J. Wang, W. Xu, Y. Yuan, W. Cai, S. Zhu, J. Zhu, *Nat. Photonics* **2016**, *10*, 393.

[23] L. Tian, J. Luan, K.-K. Liu, Q. Jiang, S. Tadepalli, M. K. Gupta, R. R. Naik, S. Singamaneni, *Nano Lett.* **2016**, *16*, 609.

[24] a) Z. L. Wang, T. Jiang, L. Xu, *Nano Energy* **2017**, *39*, 9; b) B. K. Yun, H. S. Kim, Y. J. Ko, G. Murillo, J. H. Jung, *Nano Energy* **2017**, *36*, 233; c) Z.-H. Lin, G. Cheng, S. Lee, K. C. Pradel, Z. L. Wang, *Adv. Mater.* **2014**, *26*, 4690.